# Tunable giant nonlinear optical susceptibility in math xmlns="http://www.w3.org/1998/Math/MathML">msub>mi >BaSnO/mi>mn>3/mn>/msub>/math> quantum wells

Wente Li, Ali K. Hamze, and Alexander A. Demkov

Phys. Rev. B **104**, 235419 — Published 14 December 2021

DOI: 10.1103/PhysRevB.104.235419

# Tunable giant non-linear optical susceptibility in $BaSnO_3$ quantum wells

Wente Li, Ali K. Hamze, and Alexander A. Demkov[1]

[1]Department of Physics, The University of Texas, Austin, Texas 78712, USA

## Abstract

We investigate theoretically the giant nonlinear optical susceptibilities based on intersubband transitions in the *n*-type $BaSnO_3$ quantum well heterostructures. Validity of the effective mass theory, used to compute susceptibility is demonstrated using first principles calculations. We predict $\chi^{(2)}$ values up to 200 nm/V and $\chi^{(3)}$ values up to 8000 $nm^2/V^2$, both over a much broader spectral range. $\chi^{(2)}$ is estimated from the THz region to the boundary with visible light, a range four times broader than current semiconductor quantum wells. This opens a possibility to make tunable nonlinear optical devices operating in the important range from THz to visible light.

Integrated photonics is an emerging technology combining optical and electronic properties of materials. It overcomes the limitations of traditional electronic devices, since photons can be operated at broadband with smaller loss and higher modulation speed than electrons. Hence, photonic devices have many potentially revolutionary applications. Specifically, silicon photonic devices, thanks to their excellent optical properties and natural compatibility with the CMOS processing infrastructure, have been subject to active study in recent years. These include optical modulators [1, 2], reservoir computing on a silicon photonic chip [3], inter-chip interconnects [2], quantum information processing [4, 5], and optical neuromorphic computing chips [6-8]. The use of optical nonlinearity e.g., second harmonic generation (SHG) and Pockels effect in $BaTiO_3$ on Si [9-13], or $LiNbO_3$ on Si [14-18] offers a promising path towards on-chip low power electro-optic functionality [19] for example, in edge computing.

In general, the intrinsic optical nonlinearity in most bulk materials is quite small. Typical magnitudes of the second-order optical susceptibility $\chi^{(2)}$ and the third-order $\chi^{(3)}$ are 10-

---

[1] demkov@physics.utexas.edu

$^{12}$ m/V and $10^{-22}$ $m^2/V^2$, respectively. To enhance the optical nonlinearity, artificially engineered semiconductor-heterostructure quantum wells (QWs) have been proposed [20-26], demonstrating infrared intersubband transitions and large dipole matrix elements [27].

As both $\chi^{(2)}$ and $\chi^{(3)}$ are proportional to the dipole matrix elements of a QW, these heterostructures can be designed to have extremely high optical nonlinearity [28]. For example, AlInAs/GaInAs QWs have been reported with $\chi^{(2)}$ ~$10^{-8}$ m/V, and $\chi^{(3)}$ ~$10^{-14}$ $m^2/V^2$ [22]. Such $\chi^{(2)}$ value can be further enhanced in an $In_{0.53}Ga_{0.47}As/Al_{0.48}In_{0.52}As$ QW combined with plasmonic metasurfaces [19]. Though the use of QW-based materials reduces the nonlinear optical conversion efficiency compared with bulk materials, the giant nonlinearity offers appealing advantages, e.g. highly compact and integrable nonlinear optical components, etc. And several groups reported the efficiency up to ~ 10% level [29]. One of the major limitations of semiconductor heterostructures, however, is that the depth of the confining potential depends on the conduction band offset, which is relatively small between most semiconductors [30]. The low QW confining depth results in fewer bound energy levels with narrower spacing, which limits the spectral range and tunability.

Intersubband transitions have been recently observed in metal-oxide-based QWs, e.g. ZnO and $SrTiO_3$, where the confinement can be very strong due to large (on the order of eV) conduction band offsets [31-39]. This would significantly increase the available spectral range. Owing to the development of epitaxial growth techniques for perovskite oxides on Si [40-43], it is now possible to integrate perovskite-oxide-based (PO-based) QWs with Si to make integrated silicon photonic devices [38]. For example, the $LaAlO_3/SrTiO_3$ system (LAO/STO) supports multiple QWs [36, 37] and indeed, has been directly integrated on a Si wafer [38]. Despite this remarkable success, one clear shortcoming of the LAO/STO system is the relatively large effective mass in La-doped STO ($m^*$~ $0.999m_0$) [44, 45], compared with GaInAs $m^* = 0.043m_0$ or AlInAs $m^* = 0.07m_0$ [22]. The larger effective mass results in a smaller energy spacing between the quantized energy levels, negating the advantages of a large well depth.

In this paper, we demonstrate that the PO-based QWs with the right choice of a metal oxide can significantly exceed the current semiconductor QWs nonlinearity and tunability. To this end, we propose stannate-based QWs. We use La-doped $BaSnO_3$ (BSO) as an example, where the large curvature of the Sn 5*s*-based conduction band (CB) bottom results in a very small effective mass. For bulk perovskite BSO we calculate the electron effective mass of $m^*=0.17m_0$, in good agreement with other first-principles calculations [46] and experimental value of $0.19m_0$ [47]. This choice maintains the advantage of a large CB offset (~ 1.74 eV), while alleviating the high effective mass limitation of the LAO/STO system.

To demonstrate the potential of BSO in heterostructures with highly nonlinear and field-tunable optical properties, we compute nonlinear optical response of stannate-based QWs using effective mass theory (EMT). The optimization of large-scale (> 10 nm) heterostructures requires fast and accurate calculations of the electronic structure, which is done more efficiently with a mesoscopic model. The validity of this approach is established using a multiscale simulation (details can be found in the Supplemental Material Sec. I [48]), combining atomic-level, first principles density functional theory (DFT) and a maximally localized Wannier function (WF) [49] tight-binding (TB) calculations [50] with a mesoscopic level Poisson-Schrödinger (PS) solver [34, 39, 51].

To explore $\chi^{(2)}$ and $\chi^{(3)}$ of the BSO QW heterostructures, we consider asymmetric double QWs (DQWs) and triple QWs (TQWs), since nonlinear susceptibility vanishes in symmetric single wells. Our DQW includes four- and seven-unit-cell thick BSO wells, separated by a one-unit-cell thick BaO barrier (Fig. 1), while the TQW includes three-, four-, and six-unit-cell thick BSO wells, separated by two one-unit-cell thick BaO barriers (Fig. 2). Both the DQW and the TQW are placed between thick BaO barrier layers. The calculation details for the BSO/BaO DQW and TQW are discussed in the Supplemental Material Sec. II, VII and VIII [48].

EMT [52] connects the mesoscopic and microscopic level simulations and has been widely used to describe semiconductor heterostructures [53, 54]. Its applicability depends on meeting the Luttinger criterion that the characteristic length of the potential spatial variation is much larger than the material's lattice constant [52]. Though this assumption may not be strictly true in our case, given that our inter-well barriers are one-unit-cell thick, we find overall good agreement between the mesoscopic and microscopic models, validating the approximation. In EMT, a QW is modeled as a 1D, external, scalar potential $U(z)$ (z is along the direction of confinement) imposed on the crystal periodic potential. $U(z)$ comes from the conduction band profile across the heterostructure. If the Luttinger criteria is satisfied, and $U(z)$ varies much more slowly than the atomic potential, one can separate the slow envelope function (EF) $F_n(z)$, from the rapidly varying wave function and focus on the EF only [52, 55].

It is instructive to compare the EFs in the oxide heterostructure from both, the microscopic and mesoscopic perspectives. Our mesoscopic model uses a PS solver [51] that includes the effect of La doping (see Supplemental Material Sec. V [48]). Figs. 1 and 2 show the potential profile (including the effect of doping electrons) and wave functions (solid red lines) of the DQW and TQW structures computed with the PS solver. The microscopic simulation results are based on the wave functions computed using DFT and the WF TB model. DFT implemented using the plane-wave basis (PWB) expansion of the wave functions offers a "global picture" [49] and gives the electronic structure in the momentum space. To visualize the QW EFs in real space using these "global" wave functions, we plot the charge density distribution computed using DFT within a narrow energy window around the QW bands. In Figs. 3 and 4, we show the charge density corresponding to the first and second excited state of the DQW and TQW, respectively. The brightness of the blue color is proportional to the magnitude of EFs. The overall shape of the charge density agrees rather well with the EFs computed with the PS solver.

To further explore the validity of the EMT, we use maximally-localized WFs [49, 57, 58] to construct a TB model and capture the real space information of the EFs so that we can directly compare the shape of the WFs with the charge distribution calculated within DFT, as well as wave functions from the PS solver, where the EFs are described at the mesoscopic level. Using the WF basis, we construct the projector operator for the Sn atom *s*-orbitals. Acting with it on the QW state wave functions that can be described by both TB model and in the PWB as $\psi = \sum_{\boldsymbol{G}} c(\boldsymbol{k}-\boldsymbol{G})e^{i(\boldsymbol{k}-\boldsymbol{G})\cdot\boldsymbol{r}}$ (details in the Supplemental Material Sec. IV [48]), we can extract the projected magnitudes of the EFs of the WF TB model at each Sn site. The ground state and up to the third-excited QW states EFs are shown in Figs. 1(b) and 2(b) with blue hollow dots. In Figs. 1(c) and 2(c), we show the *s*-

like WFs localized at each Sn site for the first and second excited states of the DQW and TQW, respectively. In the WF plot, red is positive, blue is negative and the size of the WFs represents the magnitude of EFs. WF magnitudes modulated by EFs agree well with the charge density distributions in Fig. 3 and 4. In Fig. 1(a), the energy differences between the levels computed with the PS solver and DFT are listed on the left and right side of the figure, respectively. For the DQW the energy differences computed with different methods are very similar (the agreement is more accurate for the lower energy states). The EF magnitudes (blue circles) derived using the maximally localized WFs agree well with the value of the PS wave function on the corresponding atomic plane. For the TQW, the energy differences and shapes of the EFs between mesoscopic and microscopic simulations are in qualitative agreement. It is important to note that the energy separation of the QW states and the shape of the EFs are very sensitive to the exact QW potential profile when using the PS solver. The rapid variation of the local electrostatic potential across the QW and the well-known band gap underestimation problem of the semi-local DFT present a bit of a challenge for the simulation. These, however, can be dealt with using standard techniques (details can be found in the Supplemental Material Sec. III [48]). Overall, the mesoscopic and microscopic simulations agree with each other, establishing the validity of EMT for BSO/BaO QWs.

With this knowledge of the confined states, we are ready to explore the optical nonlinearity of the QWs. There are multiple ways to calculate the non-linear susceptibility using *ab initio* methods e.g., time-dependent DFT [59]. Also, Sipe *et al.* [60, 61] and Segall *et al.* [62] have developed analytical expressions for the frequency dependent SHG susceptibility using perturbation theory. However, as these methods are designed for bulk crystals with relatively few atoms in the unit cell, they are not well suited for the large heterostructures like the DQW in Fig. 2(a) or TQW depicted in Fig 3(a). To compute the nonlinear susceptibility of our BSO/BaO QWs, we will leave aside the intraband transitions and focus only on the QW-induced sub-bands. Our spectrum then, using the EMT, consists of the bound QW states $E_{n,z}$ and 2D free electron bands in the directions normal to the confinement direction:

$$E_n = E_{n,z} + \frac{\hbar^2}{2m_*} k_\parallel^2. \qquad (1)$$

As shown in Figs. S5 and S9, the QW electronic structure indeed has non-dispersive (flat) bands along the *z*-direction and approximately parabolic bands in the direction normal to the well stacking in good agreement with the EMT spectrum of Eq. (1). Refs. [60-62] determine $\chi^{(2)}$ of undoped materials by integrating $\chi^{(2)}(\boldsymbol{k})$ over the Brillouin zone $\chi^{(2)} \sim \int \mathrm{d}\boldsymbol{k}\ \chi^{(2)}(\boldsymbol{k})$. $\chi^{(2)}(\boldsymbol{k})$ depends on the band structure and is sampled over special points in the Brillouin zone. However, in a lightly doped QW, we can omit the $\boldsymbol{k}$ dependence of $\chi^{(2)}(\boldsymbol{k})$ [63]. This is possible because the $\overrightarrow{k_{\parallel}}$ energy dispersion of the QW bands (shown in Figs. S5, S9) of Eq. (1) follow the same parabolic pattern, and the energy difference $\omega_{nl} = (E_n - E_l)/\hbar$ between the bands is independent of the momentum for vertical transitions [63] for low doping density. Hence, $\chi^{(2)}_{ijk}$ can be written as:

$$\chi^{(2)}_{ijk}(2\omega,\omega,\omega) = \frac{N_e}{\epsilon_0 \hbar^2} \sum\nolimits_{lmn} \left(\rho^{(0)}_{ll} - \rho^{(0)}_{mm}\right) \times \left(\mu^{i}_{ln}\mu^{j}_{nm}\mu^{k}_{ml}\right) \times \left\{\frac{1}{(\omega_{nl}-2\omega-i\gamma_{nl})(\omega_{ml}-\omega-i\gamma_{ml})} + \frac{1}{(\omega_{nm}+2\omega+i\gamma_{nl})(\omega_{ml}-\omega-i\gamma_{ml})}\right\} \qquad (2),$$

where $N_e$ is the average doping density, $\mu$ the dipole matrix and $\rho$ the density matrix. Details of calculating $\chi^{(2)}_{ijk}$ and $\chi^{(3)}_{kjih}$ are provided in the Supplemental Material Sec. VI [48]. We include a damping term, $\gamma_{nl}$, describing excited electrons in other non-QW bands, intraband motion, etc., resulting in an effective dephasing effect in the intersubband transition [64, 60-62].

The selection rule for the intersubband transitions in QWs [32, 65, 66] dictates that the intersubband transitions can only be excited by light polarized along the $\boldsymbol{z}$ direction with non-zero electric field component $\boldsymbol{E_z}$. Therefore, in the following discussion, we focus on $\chi^{(2)}_{zzz}$ and $\chi^{(3)}_{zzzz}$. In Figs. 5(a) and 5(c), we show $\left|\chi^{(2)}_{zzz}(2\omega,\omega,\omega)\right|$ and $\left|\chi^{(3)}_{zzzz}(3\omega,\omega,\omega,\omega)\right|$, for our QWs, respectively. Here, $\omega$ is the incident pump frequency and, $2\omega$ and $3\omega$ are the output frequencies. In Fig. 5(a), the spectrum of our DQW is shown in blue, and the spectrum of our TQW is shown in green. The red spectrum in Fig. 5(a) is that of an additional DQW with three- and six-unit-cell thick BSO wells. For comparison with semiconductor QWs, the magnitude of the reported $\chi^{(2)}_{zzz}$ from Ref. [19] and $\chi^{(3)}_{zzzz}$ from Ref. [22] are indicated with the black dashed lines in Figs. 5(a) and 5(c), respectively. To model doped QWs with only the ground state occupied, we use average doping densities of $N_e = 10^{19}$ cm$^{-3}$ [67] for the DQW and $N_e = 5 \times 10^{18}$ cm$^{-3}$ for the TQW. We set $\gamma_{nl} = 10$ meV for the damping term (compare with $\gamma_{nl} = 7.5 - 8.5$ meV in Ref. [19]). To maximize the SHG and THG susceptibility, the QW energy levels should be equally spaced. When this is achieved, $\left|\chi^{(2)}_{zzz}(2\omega,\omega,\omega)\right|$ and $\left|\chi^{(3)}_{zzzz}(3\omega,\omega,\omega,\omega)\right|$ are resonantly enhanced. Therefore, good control of the width of the BSO and BaO layers is necessary to tune the intersubband transitions. Since the lattice parameters of BSO and BaO are fixed, the tuning of the QW width is discrete up to half-unit-cell, meaning the energy gap changes with the width discretely instead of continuously. However, a continuous control of the gaps can be achieved *via* the Stark effect, by applying an external bias across the entire structure along the ***z***-direction [22, 39].

As shown in Fig. 1 and Fig. 2, both the micro- and mesoscopic simulations suggest that the energy differences between the QW bands are not equal. Therefore, as indicated by the solid blue line in Fig. 5(a), the unequal band spacing forms the off-resonant condition and splits $\left|\chi^{(2)}_{zzz}(2\omega,\omega,\omega)\right|$ spectrum into two peaks near 0.25 eV. Even so, the intrinsic $\chi^{(2)}_{zzz}$ is comparable with that reported in Ref. [19]. However, if we apply an external bias to tune the scalar potential profile $U(z)$ of QW and correspondingly shift the energy gaps, we observe giant $\chi^{(2)}_{zzz}$ up to 200 nm/V and 100 nm/V under negative and positive bias, respectively (blue, dashed peaks). We call the center pump frequency of $\chi^{(2)}_{zzz}$ peak the “operating frequency” (OF). A schematic of the electron excitation and relaxation processes during SHG with 0.55 eV OF is shown with the red arrows in the top panel of Fig. 5(b) and with 0.25 eV OF with the black arrows. Because PO-based QWs are much deeper than those made of semiconductors and therefore hold more quantum levels, multiple OFs are possible. The series of spectra represented by blue lines in Fig. 5(a) demonstrate that by shifting the external bias, we can shift the OFs of the QW while maintaining giant nonlinear susceptibility. Thus, one can use external bias to tune the OF, allowing to turn the SHG or THG on or off, and to enhance the susceptibility. The red spectrum in Fig. 5(a) is a different DQW, with thinner BSO wells than the DQW described in Fig. 1, showing that varying the well and barrier widths offers another way to tune the susceptibility and OFs. Also shown in Fig. 5(a) is the spectrum of TQW $\chi^{(2)}_{zzz}$ (in green), indicating the versatility of TQW, which can produce both THG and SHG. There is a large gap between the two OF peaks of the TQW (SHG processes sketched with red and black arrows in the bottom panel of Fig. 5(b)). The reported OF in semiconductor QWs is usually ~150 meV and the output is in the range of infrared radiation (~300 meV) [19, 22]. Fig. 5(a) demonstrates that the OF of the PO-based DQW and TQW ranges from 0 to 600 meV and the QWs can emit photons with energy up to 1200 meV, which is near the range of visible light.

In Fig. 5(c) we show the spectrum of $\left|\chi^{(3)}_{zzzz}(3\omega,\omega,\omega,\omega)\right|$. We see that without external bias, $\chi^{(3)}_{zzzz}(3\omega,\omega,\omega,\omega)$ is off-resonance. Applying external bias of $E_z$ = -100 kV/cm, we can bring $\chi^{(3)}_{zzzz}(3\omega,\omega,\omega,\omega)$ in resonance. Thus, $|\chi^{(3)}_{zzzz}(3\omega,\omega,\omega,\omega)|$ is comparable with Ref. [22], but with a larger OF of ~200 meV and output photon energy of 600 meV. Of course, the external bias we apply in both DQW and TQW cases is much lower than the BSO breakdown field (~ 2 MV/cm).

In conclusion, we propose a solution to address the limitations of both the semiconductor and current PO-based QWs. Using BSO for the well layer of the heterostructure yields a small effective mass with a very large conducting band offset. The latter results in large well depths and enables greater control of the QW properties. The giant nonlinear optical susceptibility is estimated up to four times larger than that reported for the semiconductor QWs [19]. The nonlinearity exists across a broad spectral range, making BSO QWs applicable at frequencies from THz to near-visible light. The strong optical nonlinearity in BaO/BSO QWs demonstrates the advantages of PO-based QWs over their semiconductor counterparts. In practical implementations, instead of BaO, one can use other barrier materials with even larger band gaps, such as $Al_2O_3$ [68]. The estimated conduction band offset at the BSO/$Al_2O_3$ interface is 3.5 eV [69], resulting in a deeper QW and extending the OF into the visible light region or even near UV. As suggested by Refs. [19, 32], one can design different QW stacking geometries and explore other light-QW coupling directions with other tensor components of $\chi^{(2)}_{ijk}$ and $\chi^{(3)}_{ijkl}$.

## Acknowledgements

We thank Agham Posadas, Wei Guo, Marc Reynaud, and Suyeong Jang for insightful discussions and critical reading of the manuscript. The work is supported by the Air Force Office of Scientific Research under grant FA9550-18-1-0053.

## References

[1] G. T. Reed, G. Mashanovich, F. Y. Gardes and D. J. Thomson, “Silicon optical modulators,” Nat. Phot. **4**, 518-526(2010).

[2] M. J. R. Heck, H.-W. Chen, A. W. Fang, B. R. Koch, D. Liang, H. Park, M. N. Sysak and J. E. Bowers, “Hybrid Silicon Photonics for Optical Interconnects,” IEEE Journal of Selected Topics in Quantum Electronics, **17**(2), 333–346 (2011).

[3] K. Vandoorne, P. Mechet, T. Van Vaerenbergh, M. Fiers, G. Morthier, D. Verstraeten, B. Schrauwen, J. Dambre and P. Bienstman, “Experimental demonstration of reservoir computing on a silicon photonics chip,” Nat. Comm. **5**, 3541 (2014).

[4] X. Qiang, X. Zhou, J. Wang, C. M. Wilkes, T. Loke, S. O’Gara, L. Kling, G. D. Marshall, R. Santagati, T. C. Ralph, J. B. Wang, J. L. O’Brien, M. G. Thompson and J. C. F. Matthews. "Large-scale silicon quantum photonics implementing arbitrary two-qubit processing," Nat. Phot. **12**, 534–539 (2018).

[5] F. Flamini, N. Spagnolo and F. Sciarrino. "Photonic quantum information processing: a review," Rep. Prog. Phys. **82**, 016001 (2019).

[6] J. Feldmann, N. Youngblood, C. D. Wright, H. Bhaskaran and W. H. P. Pernice, "All-optical spiking neurosynaptic networks with self-learning capabilities," Nature **569**, 208-214 (2019).

[7] Q. Zhang, H. Yu, M. Barbiero, B. Wang and M. Gu, "Artificial neural networks enabled by nanophotonics," Light: Science & Applications **8**, 42 (2019).

[8] H. Tan, Z. Ni, W. Peng, S. Du, X. Liu, S. Zhao, W. Li, Z. Ye, M. Xu, Y. Xu, X. Pi and D. Yang, "Broadband optoelectronic synaptic devices based on silicon nanocrystals for neuromorphic computing," Nano Energy **52**, 422-430 (2018).

[9] S. Abel, T. Stoferle, C. Marchiori, C. Rossel, M. D. Rossell, R. Erni, D. Caimi, M. Sousa, A. Chelnokov, B. J. Offrein and J. Fompeyrine, "A strong electro-optically active lead-free ferroelectric integrated on silicon," Nat. Comm. **4**, 1671 (2013).

[10] S. Abel, F. Eltes, J. E. Ortmann, A. Messner, P. Castera, T. Wagner, D. Urbonas, A. Rosa, A. M. Gutierrez, D. Tulli, P. Ma, B. Baeuerle, A. Josten, W. Heni, D. Caimi, L. Czornomaz, A. A. Demkov, J. Leuthold, P. Sanchis and J. Fompeyrine, "Large Pockels effect in micro- and nanostructured barium titanate integrated on silicon," Nat. Mat. **18**, 42-47 (2019).

[11] F. Eltes, G. E. Villarreal-Garcia, D. Caimi, H. Siegwart, A. A. Gentile, A. Hart, P. Stark, G. D. Marshall, M. G. Thompson, J. Barreto, J. Fompeyrine and S. Abel, "An integrated optical modulator operating at cryogenic temperatures," Nat. Mat. **19**, 1164–1168 (2020).

[12] K. J. Kormondy, S. Abel, F. Fallegger, Y. Popoff, P. Ponath, A. B. Posadas, M. Sousa, D. Caimi, H. Siegwart, E. Uccelli, L. Czornomaz, C. Marchiori, J. Fompeyrine, and A. A. Demkov, "Analysis of the Pockels effect in ferroelectric barium titanate thin films on Si(001)," Microelectronic Engineering **147**, 215-218 (2015).

[13] K. J. Kormondy, Y. Cho, A. B. Posadas, L. Zheng, K. Lai, Q. Wang, M. J. Kim, Q. He, A. Y. Borisevich, M. C. Downer and A. A. Demkov, "Piezoelectric modulation of nonlinear optical response in $BaTiO_3$ thin film," Appl. Phys. Lett. **113**, 132902 (2018).

[14] L. Chen, and R.M. Reano, “Compact electric field sensors based on indirect bonding of lithium niobate to silicon microrings,” Opt. Express **20**, 4032 (2012).

[15] L. Chen, Q. Xu, M.G. Wood, and R.M. Reano, "Hybrid silicon and lithium niobate electro-optical ring modulator," Optica **1**, 112 (2014).

[16] C. Wang, M. Zhang, B. Stern, M. Lipson, and M. Lončar, "Nanophotonic lithium niobate electro-optic modulators," Opt. Express **26**, 1547 (2018).

[17] C. Wang, M. Zhang, X. Chen, M. Bertrand, A. Shams-Ansari, S. Chandrasekhar, P. Winzer and M. Lončar, "Integrated lithium niobate electro-optic modulators operating at CMOS-compatible voltages," Nature **562**, 101 (2018).

[18] B. Desiatov and M. Lončar, "Silicon photodetector for integrated lithium niobate photonics," Appl. Phys. Lett. **115**, 121108 (2019).

[19] J. Lee, M. Tymchenko, C. Argyropoulos, P.-Y. Chen, F. Lu, F. Demmerle, G. Boehm, M.-C. Amann, A. Alù and M. A. Belkin, “Giant nonlinear response from plasmonic metasurfaces coupled to intersubband transitions,” Nature **511**, 65-60 (2014).

[20] M. M. Fejer, S. J. B. Yoo, R. L. Byer, Alex Harwit, and J. S. Harris Jr., “Observation of extremely large quadratic susceptibility at 9.6–10.8 μm in electric-field-biased AlGaAs quantum wells,” Phys. Rev. Lett. **62**, 1041–1044 (1989).

[21] E. Rosencher, P. Bois, J. Nagle and S. Delaitre, “Second harmonic generation by intersubband transitions in compositionally asymmetrical MQWs,” Electron. Lett. **25**, 1063–1065 (1989).

[22] F. Capasso, C. Sirtori and A. Y. Cho, “Coupled-quantum-well semiconductors with giant electric-field tunable nonlinear-optical properties in the infrared,” IEEE J. Quantum Electron. **30**, 1313–1326 (1994).

[23] E. Rosencher, A. Fiore, B. Vinter, V. Berger, Ph. Bois and J. Nagle, “Quantum engineering of optical nonlinearities,” Science **271**, 168–173 (1996).

[24] C. Gmachl, A. Belyanin, D. L. Sivco, M. L. Peabody, N. Owschimikow, A. M. Sergent, F. Capasso, and A. Y. Cho, “Optimized second-harmonic generation in quantum cascade lasers,” IEEE J. Quantum Electron. **39**, 1345–1355 (2003).

[25] M. A. Belkin, F. Capasso, A. Belyanin, D. L. Sivco, A. Y. Cho, D. C. Oakley, C. J. Vineis and G. W. Turner, “Terahertz quantum-cascade-laser source based on intracavity difference-frequency generation,” Nat. Phot. **1**, 288–292 (2007).

[26] K. Vijayraghavan, Y. Jiang, M. Jang, A. Jiang, K. Choutagunta, A. Vizbaras, F. Demmerle, G. Boehm, M. C. Amann and M. A. Belkin, “Broadly tunable terahertz generation in mid-infrared quantum cascade lasers,” Nat. Comm. **4**, 2021 (2013).

[27] L. C. West and S. J. Eglash, “First observation of an extremely large dipole infrared transition within the conduction band of a GaAs quantum well,” Appl. Phys. Lett., **46**, 1156-1157 (1985).

[28] M. Gurnick and T. DeTemple, "Synthetic nonlinear semiconductors," IEEE J. Quantum Electron. QE-**19**, 791 (1983).

[29] I. Vurgaftman, J. R. Meyer and L. R. Ram-Mohan, "Optimized second-harmonic generation in asymmetric double quantum wells," IEEE J. of Quantum Electronics **32**, 8 (1996).

[30] C. G. Van de Walle and R. M. Martin, "Theoretical study of band offsets at semiconductor interfaces," Phys. Rev. B **35**, 8154 (1987).

[31] B. Meng, J. Tamayo-Arriola, N. Le Biavan, M. M. Bajo, A. Torres-Pardo, M. Hugues, D. Lefebvre, A. Hierro, J.-M. Chauveau and J. Faist, "Observation of Intersubband Absorption in ZnO Coupled Quantum Wells," Phys. Rev. Appl. **12**, 054007 (2019).

[32] M. Montes Bajo, J. Tamayo-Arriola, N. Le Biavan, J. M. Ulloa, P. Vennéguès, D. Lefebvre, M. Hugues, J.-M. Chauveau, and A. Hierro, "Breaking the Intersubband Selection Rules for Absorption with ZnO Quantum Wells: Light Polarization Sensitivity under Normal Incidence," Phys. Rev. Appl. **10**, 034022 (2018).

[33] C. Lin, A. B. Posadas, M. Choi, and A. A. Demkov, “Optical properties of transition metal oxide quantum wells,” J. Appl. Phys. **117**, 034304 (2015).

[34] M. Choi, C. Lin, M. Butcher, C. Rodriguez, Q. He, A. B. Posadas, A. Y. Borisevich, S. Zollner, and A. A. Demkov, “Quantum confinement in transition metal oxide quantum wells,” Appl. Phys. Lett. **106**, 192902 (2015).

[35] L. Bjaalie, B. Himmetoglu, L. Weston, A. Janotti and C. G. Van de Walle, "Oxide interfaces for novel electronic applications," New J. Phys. **16**, 025005 (2014).

[36] J. E. Ortmann, A. B. Posadas and A. A. Demkov, “The MBE growth of arbitrarily thick $SrTiO_3/LaAlO_3$ quantum well heterostructures for use in next-generation optoelectronic devices,” J. Appl. Phys. **124**, 015301 (2018).

[37] J. E. Ortmann, N. Nookala, Q. He, L. Gao, C. Lin, A. B. Posadas, A. Y. Borisevich, M. A. Belkin, and A. A. Demkov, “Quantum confinement in oxide heterostructures: Room-temperature intersubband absorption in $SrTiO_3/LaAlO_3$ multiple quantum wells,” ACS NANO **12**, 7682 (2018).

[38] J. E. Ortmann, S. Kwon, A. B. Posadas, M. J. Kim and A. A. Demkov, “Monolithic Integration of Transition Metal Oxide Multiple Quantum Wells on Silicon (001),” J. Appl. Phys. **125**, 155302 (2019).

[39] J. E. Ortmann, M. A. Duncan and A. A. Demkov, "Designing near-infrared electro-optical devices from the $SrTiO_3/LaAlO_3$ materials system," Opt. Mater. Express **9**, 2982−2993 (2019).

[40] R. A. McKee, F. J. Walker, and M. F. Chisholm, "Crystalline Oxides on Silicon: The First Five Monolayers," Phys. Rev. Lett. **81**, 3014 (1998).

[41] R. A. McKee, F. J. Walker, and M. F. Chisholm, "Physical Structure and Inversion Charge at a Semiconductor Interface with a Crystalline Oxide," Science **293**, 468-471 (2001).

[42] D. P. Kumah, J. H. Ngai and L. Kornblum, "Epitaxial Oxides on Semiconductors: From Fundamentals to New Devices," Adv. Funct. Mater. **30**, 1901597 (2020).

[43] A. A. Demkov and A. B. Posadas, *Integration of functional oxides with semiconductors*, (Springer, New York, 2014).

[44] M. Choi, A. B. Posadas, C. A. Rodriguez, A. O'Hara, H. Seinige, A. J. Kellock, M. M. Frank, M. Tsoi, S. Zollner, V. Narayanan, and A. A. Demkov, "Structural, optical, and electrical properties of strained La-doped $SrTiO_3$ films," J. Appl. Phys. **116**, 043705 (2014).

[45] A. F. Santander-Syro, O. Copie, T. Kondo, F. Fortuna, S. Pailhès, R. Weht, X. G. Qiu, F. Bertran, A. Nicolaou, A. Taleb-Ibrahimi, P. Le Fèvre, G. Herranz, M. Bibes, N. Reyren, Y. Apertet, P. Lecoeur, A. Barthélémy and M. J. Rozenberg, "Two-dimensional electron gas with universal subbands at the surface of $SrTiO_3$,” Nature **469**, 189–193 (2011).

[46] Y. Kang, H. Peelaers, K. Krishnaswamy, and C. G. Van de Walle, "First-principles study of direct and indirect optical absorption in $BaSnO_3$,” Appl. Phys. Lett. **112**, 062106 (2018).

[47] C. A. Niedermeier, S. Rhode, K. Ide, H. Hiramatsu, H. Hosono, T. Kamiya, and M. A. Moram, "Electron effective mass and mobility limits in degenerate perovskite stannate $BaSnO_3$,” Phys. Rev. B **95**, 161202(R) (2017).

[48] See Supplemental Material at [URL will be inserted by publisher] for details.

[49] N. Marzari, A. A. Mostofi, J. R. Yates, I. Souza, and D. Vanderbilt, "Maximally localized Wannier functions: Theory and applications," Rev. Mod. Phys. **84**, 1419 (2012).

[50] G. Pizzi, V. Vitale, R. Arita, S. Blügel, F. Freimuth, G. Géranton, M. Gibertini, D. Gresch, C. Johnson, T. Koretsune, J. Ibañez-Azpiroz, H. Lee, J.-M. Lihm, D. Marchand, A. Marrazzo, Y. Mokrousov, J. I. Mustafa, Y. Nohara, Y. Nomura, L. Paulatto, S. Poncé, T. Ponweiser, J. Qiao, F. Thöle, S. S Tsirkin, M. Wierzbowska, N. Marzari, D. Vanderbilt, I. Souza, A. A Mostofi, and J. R Yates, “Wannier90 as a community code: new features and applications,” J. Phys.: Condens. Matter **32**, 165902 (2020).

[51] P. Harrison and A. Valavanis, *Quantum Wells, Wires and Dots: Theoretical and Computational Physics of Semiconductor Nanostructures,* 4th ed. (John Wiley and Sons, New York, 2016).

[52] J. M. Luttinger and W. Kohn, "Motion of Electrons and Holes in Perturbed Periodic Fields," Phys. Rev. **97**, 869 (1955).

[53] C. Priester, G. Allan, and M. Lannoo, "Validity of the effective-mass approximation for shallow impurity states in narrow superlattices," Phys. Rev. B **28**, 7194 (1983).

[54] G. T. Einevoll, "Operator ordering in effective-mass theory for heterostructures. II. Strained systems," Phys. Rev. B **42**, 3497 (1990).

[55] C. Jacoboni, *Theory of Electron Transport in Semiconductors,* Springer-Verlag Berlin Heidelberg (2010).

[56] P. Harrison and A. Valavanis, *Quantum Wells, Wires and Dots: Theoretical and Computational Physics of Semiconductor Nanostructures*, 4th ed. (John Wiley and Sons, New York, 2016).

[57] C. Wang, X. Liu, L. Kang, B.-L. Gu, Y. Xu, and W. Duan, "First-principles calculation of nonlinear optical responses by Wannier interpolation," Phys. Rev. B **96**, 115147 (2017).

[58] T. Dumitrică, J. S. Graves, and R. E. Allen, "Second-order susceptibility from a tight-binding Hamiltonian," Phys. Rev. B **58**, 15340 (1998).

[59] E. Luppi, H. Hübener, and V. Véniard, "Ab initio second-order nonlinear optics in solids: Second-harmonic generation spectroscopy from time-dependent density-functional theory," Phys. Rev. B **82**, 235201 (2010).

[60] C. Aversa and J. E. Sipe, "Nonlinear optical susceptibilities of semiconductors: Results with a length-gauge analysis," Phys. Rev. B **52**, 14636 (1995).

[61] J. L. P. Hughes and J. E. Sipe, "Calculation of second-order optical response in semiconductors," Phys. Rev. B **53**, 10751 (1996).

[62] S. N. Rashkeev, W. R. L. Lambrecht, and B. Segall, "Efficient ab initio method for the calculation of frequency-dependent second-order optical response in semiconductors," Phys. Rev. B **57**, 3905 (1998).

[63] L. C. Lew Yan Voon and L. R. Ram-Mohan, "Calculations of second-order nonlinear optical susceptibilities in III-V and II-VI semiconductor heterostructures," Phys. Rev. B **50**, 14421 (1994).

[64] R. W. Boyd, Nonlinear Optics, 3rd ed. (Elsevier, San Diego, 2008).

[65] H. C. Liu, M. Buchanan, and Z. R. Wasilewski, "How good is the polarization selection rule for intersubband transitions?" Appl. Phys. Lett. **72**, 1682 (1998).

[66] R. Q. Yang, J. M. Xu, and M. Sweeny, "Selection rules of intersubband transitions in conduction-band quantum wells," Phys. Rev. B **50**, 7474 (1994).

[67] H. J. Kim, U. Kim, T. H. Kim, J. Kim, H. M. Kim, B.-G. Jeon, W.-J. Lee, H. S. Mun, K. T. Hong, J. Yu, K. Char, and K. H. Kim, "Physical properties of transparent perovskite oxides (Ba,La)$SnO_3$ with high electrical mobility at room temperature," Phys. Rev. B **86**, 165205 (2012).

[68] C. Park, U. Kim, C. J. Ju, J. S. Park, Y. M. Kim, and K. Char, "High mobility field effect transistor based on $BaSnO_3$ with $Al_2O_3$ gate oxide," Appl. Phys. Lett. **105**, 203503 (2014).

[69] W. Guo, S. Jang, W. Li and A. A. Demkov, unpublished.

## Supplemental material references

[1] G. Kresse and J. Hafner, "Ab initio molecular dynamics for liquid metals," Phys. Rev. B **47**, 558(R) (1993).

[2] G. Kresse and J. Furthmüller, "Efficient iterative schemes for ab initio total-energy calculations using a plane-wave basis set," Phys. Rev. B **54**, 11169 (1996).

[3] G. Kresse and J. Furthmüller, "Efficiency of ab-initio total energy calculations for metals and semiconductors using a plane-wave basis set," Comput. Mat. Sci. **6**, 15 (1996).

[4] G. Kresse and D. Joubert, "From ultrasoft pseudopotentials to the projector augmented-wave method," Phys. Rev. **B** 59, 1758 (1999).

[5] G. Pizzi, V. Vitale, R. Arita, S. Blügel, F. Freimuth, G. Géranton, M. Gibertini, D. Gresch, C. Johnson, T. Koretsune, J. Ibañez-Azpiroz, H. Lee, J.-M. Lihm, D. Marchand, A. Marrazzo, Y. Mokrousov, J. I. Mustafa, Y. Nohara, Y. Nomura, L. Paulatto, S. Poncé, T. Ponweiser, J. Qiao, F. Thöle, S. S Tsirkin, M. Wierzbowska, N. Marzari, D. Vanderbilt, I. Souza, A. A Mostofi, and J. R Yates, “Wannier90 as a community code: new features and applications,” J. Phys.: Condens. Matter **32**, 165902 (2020).

[6] M. Butcher and A. Demkov, “Energy States in $LaAlO_3/SrTiO_3$ Quantum Wells,” Honors Theses Collection, the University of Texas at Austin (2015).

[7] R. M. Feenstra, N. Srivastava, Q. Gao, M. Widom, B. Diaconescu, T. Ohta, G. L. Kellogg, J. T. Robinson, and I. V. Vlassiouk, "Low-energy electron reflectivity from graphene," Phys. Rev. B **87**, 041406(R) (2013).

[8] W. Kohn and L. J. Sham, "Self-Consistent Equations Including Exchange and Correlation Effects," Phys. Rev. **140**, A1133 (1965).

[9] D. M. Ceperley and B. J. Alder, “Ground state of the electron gas by a stochastic method,” Phys. Rev. Lett. **45**, 566–569 (1980).

[10] P. E. Blöchl, "Projector augmented-wave method," Phys. Rev. B **50**, 17953 (1994).

[11] H. J. Monkhorst and J. D. Pack, "Special points for Brillouin-zone integrations," Phys. Rev. B **13**, 5188 (1976).

[12] H. J. Kim, J. Kim, T. H. Kim, W.-J. Lee, B.-G. Jeon, J.-Y. Park, W. S. Choi, D. W. Jeong, S. H. Lee, J. Yu, T. W. Noh, and K. H. Kim. "Indications of strong neutral impurity scattering in $Ba(Sn,Sb)O_3$ single crystals," Phys. Rev. B **88**, 125204 (2013).

[13] S. A. Chambers, T. C. Kaspar, A. Prakash, G. Haugstad and B. Jalan, "Band alignment at epitaxial $BaSnO_3/SrTiO_3(001)$ and $BaSnO_3/LaAlO_3(001)$ heterojunctions," Appl. Phys. Lett. **108**, 152104 (2016).

[14] Y. Kang, H. Peelaers, K. Krishnaswamy, and C. G. Van de Walle, "First-principles study of direct and indirect optical absorption in BaSnO3," Appl. Phys. Lett. **112**, 062106 (2018).

[15] C. A. Niedermeier, S. Rhode, K. Ide, H. Hiramatsu, H. Hosono, T. Kamiya, and M. A. Moram, "Electron effective mass and mobility limits in degenerate perovskite stannate BaSnO3," Phys. Rev. B **95**, 161202(R) (2017).

[16] G. Q. Lin, H. Gong, and P. Wu, "Electronic properties of barium chalcogenides from first-principles calculations: Tailoring wide-band-gap II-VI semiconductors," Phys. Rev. B 71, 085203 (2005).

[17] L. Kleinman, "Comment on the average potential of a Wigner solid," Phys. Rev. B **24**, 7412 (1981).

[18] C. G. Van de Walle and R. M. Martin, "Theoretical calculations of heterojunction discontinuities in the Si/Ge system," Phys. Rev. B 34, 5621 (1986).

[19] J. P. Perdew and M. Levy, "Physical Content of the Exact Kohn-Sham Orbital Energies: Band Gaps and Derivative Discontinuities," Phys. Rev. Lett. **51**, 1884 (1983).

[20] J. P. Perdew, “Density functional theory and the band gap problem,” Int. J. Quantum Chem. **28**(S19), 497–523 (1985).

[21] L. J. Sham and M. Schlüter, "Density-Functional Theory of the Energy Gap," Phys. Rev. Lett. **51**, 1888 (1983).

[22] R. W. Boyd, Nonlinear Optics, 3rd ed. (Elsevier, San Diego, 2008).

[23] C. Aversa and J. E. Sipe, "Nonlinear optical susceptibilities of semiconductors: Results with a length-gauge analysis," Phys. Rev. B **52**, 14636 (1995).

[24] J. L. P. Hughes and J. E. Sipe, "Calculation of second-order optical response in semiconductors," Phys. Rev. B **53**, 10751 (1996).

[25] S. N. Rashkeev, W. R. L. Lambrecht, and B. Segall, "Efficient ab initio method for the calculation of frequency-dependent second-order optical response in semiconductors," Phys. Rev. B **57**, 3905 (1998).

# Figures

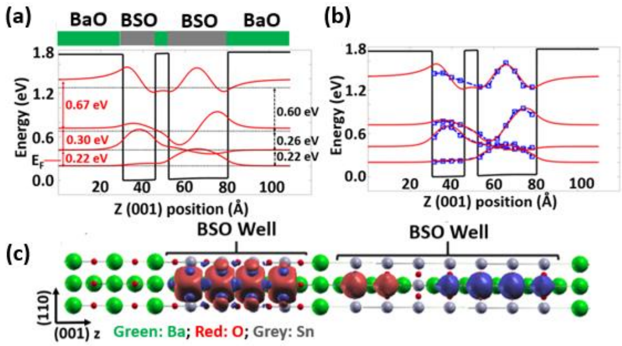

Fig. 1 (a) Schematic of DQW and mesoscopic simulation wave function results (red solid line). The Fermi level, which is in the conduction band due to the La doping density of $10^{19}$ cm$^{-3}$, is labeled with a short red line. There are four bounded quantum levels, whose band gaps are labelled by red arrows (PS solver results) and black arrows (DFT results) for comparison. (b) Comparison of mesoscopic (red) wave functions and WF (blue) results. (c) WF EFs on each Sn site of the first excited state. Details are available in the Supplemental Material Sec VII [48].

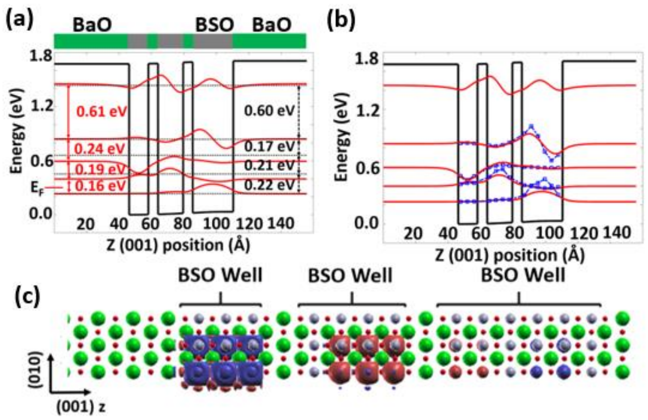

Fig. 2 (a) Schematic structure of TQW and mesoscopic simulation wave function results. The doping density used for the TQW is $5x10^{18}$ cm$^{-3.}$ The Fermi energy is labelled by $E_F$. Energy gaps of DFT and PS solver are displayed. (b) Comparison of mesoscopic wave functions and WF results. (c) WF EFs on each local Sn site of the second excited state. Plot colors follow Fig. 1.

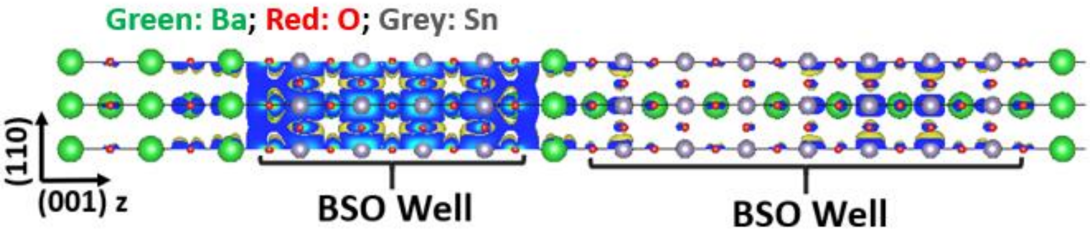

Fig. 3 DQW charge density of the first excited state from DFT.

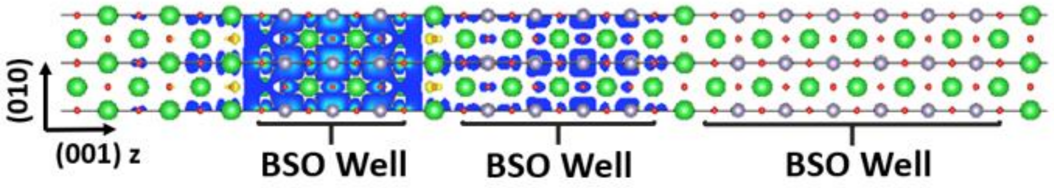

Fig. 4 TQW charge density of the second excited state from DFT.

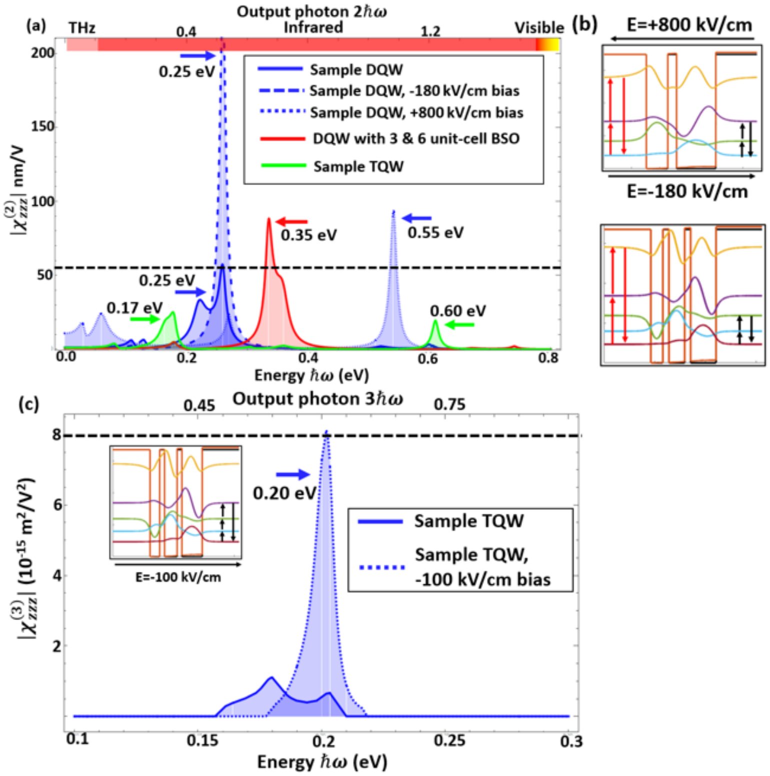

Fig. 5 SHG and THG spectra of $\chi^{(2)}_{zzz}$ and $\chi^{(3)}_{zzzz}$ with respect to incident pump frequency. (a) Three different SHG spectra colored blue, red and green. Colored arrows indicate the frequency values of the $\chi^{(2)}_{zzz}$ peak for each spectrum. (b) The top panel shows the SHG processes of the DQW, and the bottom panel shows the SHG process of the TQW. Two different SHG processes are available in the DQW and TQW. (c) THG spectra of TQW with and without external bias. Inset panel is the schematic format of THG.